

Comparison of dU/dQ , Voltage Decay, and Float Currents via Temperature Ramps and Steps in Li-Ion Batteries

Mohamed Azzam,^{*[a, b]} Moritz Ehrensberger,^[a] Christian Endisch,^[a] Dirk-Uwe Sauer,^[b, c, d, e] and Meinert Lewerenz^[a]

In this study, the effect of temperature changes on the voltage decay and current behavior of lithium-ion cells is investigated, focusing on a comparison between open-circuit voltage (OCV) measurements and float current I_{float} measurements. Using our self-developed advanced Floater system, the voltage decay rates $\frac{dU}{dT_{\text{OCV}}}$ from OCV and float current measurements for three different cell types are assessed. Temperature ramps and steps, ranging from 5 °C to 50 °C, are applied to capture the impact of entropic effects and aging mechanisms. Both methods effectively capture aging dynamics, showing strong agreement between ramp and step measurements. Deviations arise only in cases of strong entropy effects due to differences in measure-

ment strategies. The findings confirm that float currents do not introduce additional aging beyond that captured by OCV measurements. The relationship between OCV and float current is governed by differential capacity $\frac{dU}{dQ'}$ which varies with cell voltage and temperature. Furthermore, strong deviations from classical differential voltage analysis but high agreement with local pulse measurements are observed, especially at low depths of discharge. This can be explained by the hysteresis effect of graphite. These findings highlight the benefits of high-precision float current measurements in aging studies, particularly in contrast to simpler OCV methods.

1. Introduction

For long-term applications, such as electric vehicles (EVs), the target lifetime is in the order of 10 to 20 years.^[1] As the vehicles are in an idle state most of the time, besides fast charging, the lifetime is mainly determined by calendar aging.^[2] So far there are two main strategies to measure aging.^[3] One is to accelerate the aging by increasing the stress factors such as temperature and SOC with the risk of not only accelerating the aging but triggering other mechanisms that would not occur during normal operation, and thus overestimating the aging. The other option is to increase precision

and measure the aging under the mild stress factors expected during an application. In the following, we will focus on high precision measurements to assess the inherently low aging rate of lithium-ion batteries.

Historically, capacity measurements have been the standard method for evaluating calendar aging, but they have significant limitations.^[4] With increasing capacity test frequency, a calendar aging test turns to some extent into a cyclic aging test.^[5] Thus, for low aging conditions only one capacity test every one or two months is recommended. Moreover during the first weeks to months of testing, a capacity test is always and significantly influenced by reversible effects such as anode overhang.^[6–10] Finally the capacity depends on the cell dynamics due to the polarization effects stemming from increased internal resistance.^[11] Furthermore, these tests are typically conducted under constant temperature conditions ($> 20^{\circ}\text{C}$),^[12–15] which do not accurately reflect the dynamic thermal environments encountered in real-world applications. Achieving high precision in traditional capacity tests is challenging due to the superimposed reversible and dynamic effects and the very low aging rate of lithium-ion batteries especially for low temperature measurements as conducted by de Hoog et al.,^[16] Rumberg et al.,^[17] and Bouchhima et al.^[18]

A promising alternative measurement strategy to determine even extremely low self-discharge rates is the float current analysis. This technique evaluates the trickle charge during extended potentiostatic holds, attributing it to the calendar aging. Recent publications found a correlation to the capacity loss rate, as stated by Lewerenz et al.^[19] and Theiler et al.^[20] Azzam et al.^[21] identified a significant connection between the float currents and the SEI layer development, noting its pronounced influence at lower states of charge, and

[a] M. Azzam, M. Ehrensberger, C. Endisch, M. Lewerenz
Research Group Electromobility and Learning Systems, Technische Hochschule Ingolstadt, D-85049, Ingolstadt Germany
E-mail: els@thi.de

[b] M. Azzam, D.-U. Sauer
Chair for Electrochemical Energy Conversion and Storage Systems, Institute for Power Electronics and Electrical Drives (ISEA), RWTH Aachen University, Campus-Boulevard 89, 52074 Aachen, Germany

[c] D.-U. Sauer
Jülich Aachen Research Alliance, JARA-Energy, Templergraben 55, 52056 Aachen, Germany

[d] D.-U. Sauer
Institute for Power Generation and Storage Systems (PGS), E.ON ERC, RWTH Aachen University, Mathieustrasse 10, 52074 Aachen, Germany

[e] D.-U. Sauer
Helmholtz Institute Münster (HI MS), IEK-12, Forschungszentrum Jülich, 52425 Jülich, Germany

Supporting information for this article is available on the WWW under <https://doi.org/10.1002/batt.202400627>

© 2024 The Author(s). *Batteries & Supercaps* published by Wiley-VCH GmbH. This is an open access article under the terms of the Creative Commons Attribution License, which permits use, distribution and reproduction in any medium, provided the original work is properly cited.

a cathodic effect, most impactful at higher states of charge, based on the voltage slippery theory.^[22] Streck et al.^[23] and Boetticher et al.^[24] suggested that this phenomenon at higher voltages might be due to a coupled-side reaction. Alternatively, Keil et al.^[25] proposed that it could be caused by LiPF₆ decomposition. This was later confirmed by Hartmann et al.^[26] by demonstrating electrolyte decomposition through reduced salt concentration and increased active lithium at high temperatures and voltages in a post-mortem study.

A central question of the float current analysis is whether it triggers additional aging effects compared to a conventional open circuit voltage (OCV) test. OCV measurements along with the differential voltage analysis $\frac{dU}{dQ}$ have long been used to quantify lithium-ion battery self-discharge rates. Zilberman et al.^[27] and Schmidt et al.^[28] have utilized these techniques to quantify self-discharge rates related to calendar aging. Other studies utilizing OCV measurements for self-discharge rates assessment have also shown high accordance and higher aging at higher cell voltages.^[29–31] Using traditional capacity tests, Käbitz et al.^[32] found that the aging behaviors between OCV and constant voltage (CV), storage conditions differ mainly at 100% SoC. At other SoC levels, they observed no significant difference in capacity loss between OCV and CV conditions. Additionally, they identified the temperature dependency of aging as being of the Arrhenius type. Azzam et al.^[33] confirmed this, showing that during temperature ramps, float current is a superposition of aging and entropy currents, while during temperature steps, only the aging current is measured after the entropy effect decays.

This study aims to investigate whether float current measurements introduce additional aging mechanisms compared to traditional OCV measurements, while also examining the differences in aging behavior and test methodology between these two approaches under temperature variation. Therefore, we exclude the transient part stemming mainly from anode overhang by a CV phase of about 30–60 days at 30 °C before the OCV test. In our test, various cell voltages for three types of cells with varying cathode active material and cell capacity are investigated changing the temperature via steps and via ramps. For the float current analysis, the float current is evaluated, while for the OCV test, the change of voltage is measured. The transformation of one method into the other is the $\frac{dU}{dQ}$ value, which varies with cell type and SOC.

In Section 2.2.1, we present our methodology for comparing OCV to float current measurements. Section 2.2.2 provides a theoretical framework for distinguishing between entropy and aging effects via temperature ramping. In Section 3.1, we compare different temperature ramps for OCV and float current measurements. Section 3.2 examines aging outcomes from various temperature ramp methodologies using two evaluation methods. Section 3.3 details the methodology for measuring $\frac{dU}{dQ}$ to attempt to establish the equivalence of float and OCV measurements. Finally, Section 3.4 analyzes aging using the temperature steps profile to explore the OCV and float analogy via $\frac{dU}{dQ}$. Finally, we discuss whether OCV or float current analysis is superior in determining aging rates, and

whether the additional measurement effort for the float current analysis is justified.

Experimental

Experimental, Equipment and Test Setup

For this study, 12 cylindrical 18650 cells of three different cell types with graphite anode and different cathode active materials and nominal capacities are investigated. The detailed information about the test cells is given in Table 1 with the abbreviations A123, PAN and SAN that will be used in the following. The cells are tested using a self-developed measurement device for float current measurements, labelled as Floater version 2.0. Detailed specifications of the measurement device will be presented in section 2.1.1. The Keithley DMM6500 multimeter is utilized for the OCV measurements. This multimeter, equipped with a Keithley 2000 SCAN multiplexer card, serves as the measurement system. It operates in a high-impedance (~10 GΩ) mode and is positioned in a neutral position between measurement intervals. The cells are situated and tested in a Binder temperature chamber (KB115 (E4)). For the $\frac{dU}{dQ}$ measurement the –2 to +8 V/±5 A Keysight SL1004 A battery-cycler is used.

The cell voltages with three decimal places represent the cell floated at their initial storage voltage as they were delivered. The cells underwent a specific test procedure, which is presented in Figure 1.

Before the test execution, the cells are situated in a temperature-controlled chamber for a period of approximately 1 month in order to conclude the transient processes, such as polarization and anode overhang.^[6] Additionally, the cells underwent a series of prior tests and measurement procedures, which further helped minimize reversible aging effects, including polarization and anode overhang. Thereafter, the experiment starts and the OCV during a zero current phase is measured undergoing the following temperature profile shown in Figure 2. After the OCV execution, the cells are recharged back to their float voltages and are then floated in a temperature-controlled chamber for a period of 1 month for all transient processes to stabilize. This one-month duration was found to be sufficient, as demonstrated in our previous study.^[6] The constant voltage phase between the OCV and float current measurement is to assure that all reversible processes have declined and only a steady-state current is present. After this initial voltage hold period, the cells pass through the same temperature profile shown in Figure 2 while the respective float current response is being measured (Figure 3).

Table 1. Specifications of the three used battery cell types.

Short Name	A123	PAN	SAN
Producer	A123	Panasonic	Sanyo
Cell type	APR18650M-A1	NCR18650B	UR18650AAN
Cathode	LFP	NCA	NMC
Anode	Graphite	Graphite	Graphite
Nom. Capacity	1.1 Ah	3.2 Ah	2.15 Ah
Examined float voltages	3.2 V, 3.296 V, 3.4 V, 3.5 V	3.586 V, 3.7 V, 3.8 V, 4.0 V, 4.2 V	3.7 V, 3.8 V, 4.0 V

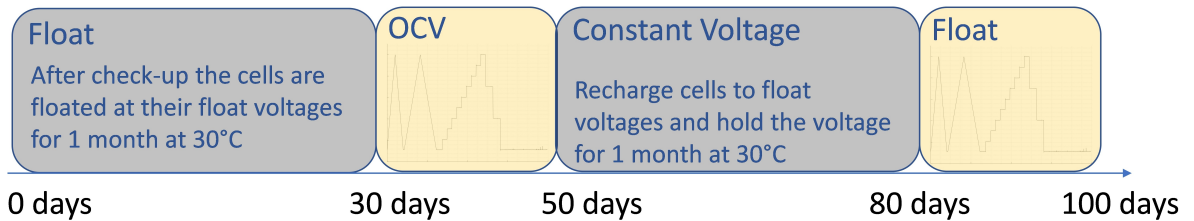


Figure 1. Measurement procedure for each cell.

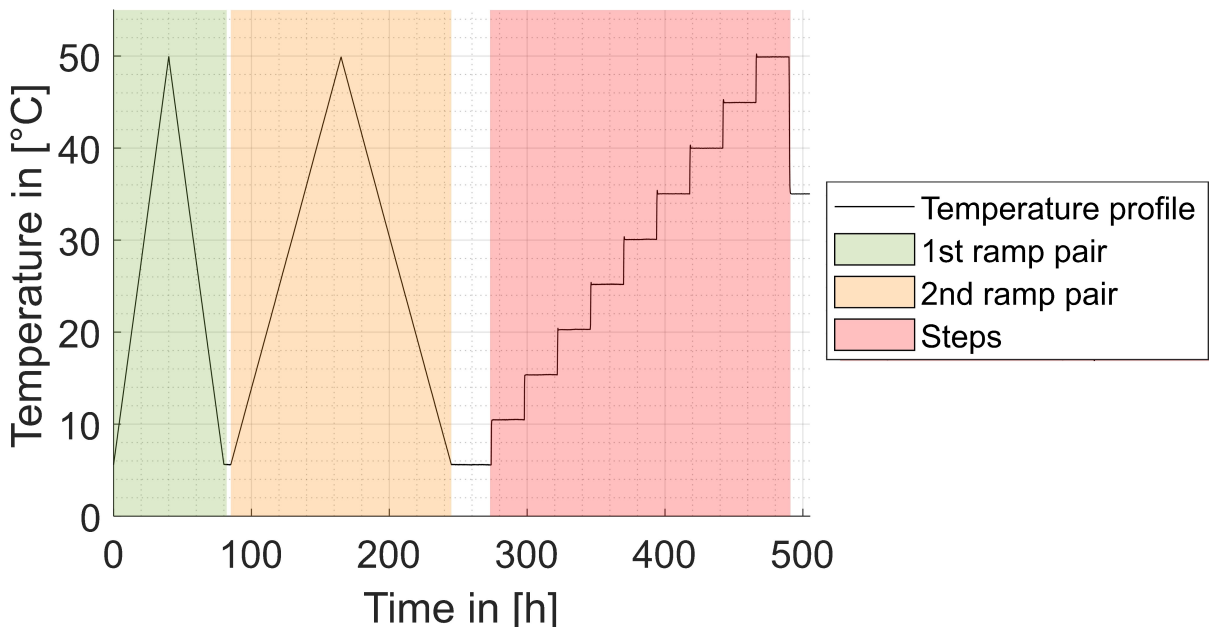


Figure 2. Temperature profile used for this study.

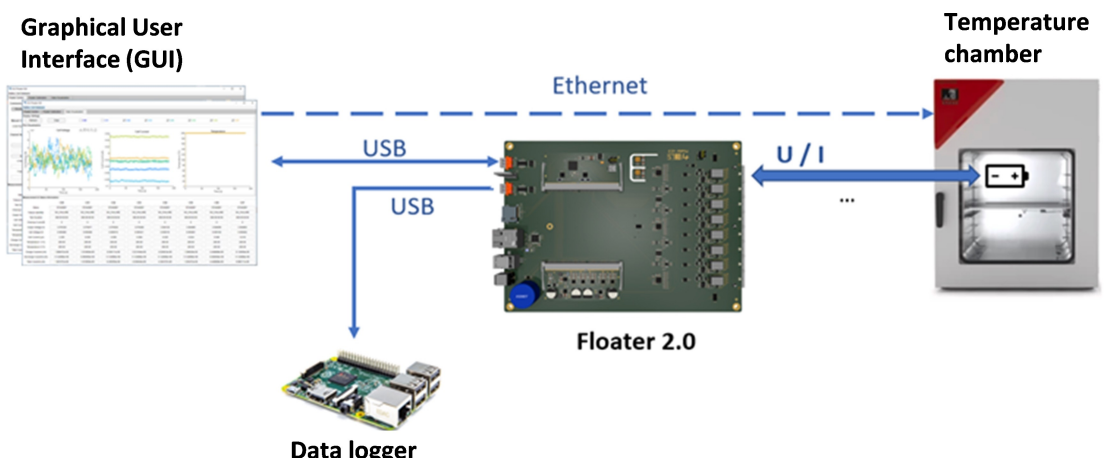


Figure 3. Floater hardware & GUI setup in the test environment.

For the OCV measurement, all 12 cells are situated in the same temperature chamber and are multiplexed to a multimeter situated in a temperature-controlled lab environment. Regarding the float procedure, the tested cells are conducted using two Floater units with 8-channels each. The first Floater comprises all four cells of the A123 and the second Floater all PAN and SAN cells. Both Floater units are situated in a temperature chamber with a constant temperature of 25°C to exclude any negative

impact due to temperature fluctuations on the high-precision measurement of the Floater hardware. The 12 cells are then situated in a separate temperature chamber undergoing the temperature profile.

The examined temperature range lies between 5 °C and 50 °C. With this, a broad temperature range of the typical usage without triggering severe aging mechanisms is covered. Thus, comparable

aging modes and no path dependency in subsequent temperature ramps are expected, as observed by Lewerenz et al.^[19] in this temperature range. In total, two temperature ramp pairs are tested. Both ramp pairs consist of an upward and a downward ramp at the same ramp speed. The first ramp pair, depicted in green in Figure 2, is executed with a ramp speed of 0.54 K/h, meaning that an upward or downward ramp takes 80 h, respectively. The second ramp pair (orange in Figure 2) is carried out at the doubled ramp speed, with a speed of 1.08 K/h and 40 h duration. The slow temperature adjustment ensures a uniform and steady temperature gradient throughout the cell, which is in the order of the control fluctuation of the chamber at constant temperature itself.

After executing the two ramp pairs, a stepwise profile is executed, depicted in red in Figure 2. The step profile increases the temperature in 5 K steps from 5 °C to 50 °C. Between each step, a hold period of 24 h is executed until the entropy effect decays and the measured float current and open circuit voltage reaches a state associated with aging only. The value is determined by calculating the mean value over the final six hours before changing the temperature to the next step.

Floater Hardware

As standard cyclers are expensive and mostly do not meet the requirements of a Floater system in terms of voltage stability and high-precision current measurement, we developed a test device on our own optimized for float current analysis called Floater system. The Floater system has an eight-channel configuration, each channel is capable of high-precision voltage (0.4 μ V_{rms}) and current measurements (1.0 nA_{rms}), complemented by one universal temperature and humidity sensors for the cells and the Floater system itself. As the temperature will remain constant or change very gradually, one sensor per unit is sufficient, provided that all cells are placed in the same temperature chamber.

The Floater system employs a four-wire measurement technique for rapid current regulation and precise voltage readings, effectively eliminating any influence of the cable resistance and float current on the voltage measurement. This upgrade, implemented in the transition from Floater versions 1.2 to 2.0, ensures independence from cable resistance issues. Additionally, before each measurement, the time constant of the wiring is evaluated to guarantee fast current regulation and minimize oscillations. While oscillations originating from the entropy effect cannot be entirely avoided, they are average-neutral and can be easily mitigated through data averaging, further enhancing measurement reliability. This consideration is critical, even though the current itself is very low, as the wiring—combined with its unknown resistance and the cells' potentially large differential capacitance—creates a low-pass characteristic with a time constant that can reach thousands of seconds.

The system incorporates a graphical user interface (GUI) to explicitly set the defined temperature profile while maintaining a constant voltage and measuring only the current response. Data integrity is a paramount feature, ensured through redundant data storage and advanced communication protocols that guarantee reliable and accurate data capture. Compared to standard test cyclers, the Floater system is a low cost and optimized test system for float current analysis. Furthermore, it is continuously optimized for the float current analysis and additional features like electrochemical impedance spectroscopy and three-electrode-measurements will be introduced soon.

Mathematical Considerations for Temperature Ramp Effects

We first start with the measured U_{OCV} , which is equal to U_0 under constant temperature assuming no aging, after allowing sufficient waiting time following the last voltage change to ensure the cell has reached equilibrium. During a rising or falling temperature ramp, the voltage changes due to aging U_{Aging} and entropy U_E must be additionally considered. The measured U_{OCV} is described as:

$$U_{OCV} = U_0 - U_{Aging} + U_E \quad (1)$$

U_E can be formulated as:

$$U_E(T^2) = U_{Nernst}(T) + U_{Fermi}(T^2) = \pm(A \cdot T + B \cdot T^2 + C) \quad (2)$$

With U_{Nernst} correlating linearly with macroscopic temperature changes in the cell, and U_{Fermi} correlating quadratically with microscopic temperature changes, as investigated by Mertin et al.^[34] C is the offset value in V, B being the quadratic slope value in $\frac{V}{K^2}$ triggered by U_{Fermi} and A being slope value in $\frac{V}{K}$ triggered by U_{Nernst} .

The measured float current I_{Float} is obtained under potentiostatic conditions. During a temperature ramp increase or decrease, the float current is a superposition of the aging current I_{Aging} and the current induced by the entropy I_E and is described as:

$$I_{Float} = I_{Aging} + I_E \quad (3)$$

With the entropy-induced current being equal to:

$$I_E = \frac{dQ}{dt} = \frac{dQ}{dU} \cdot \frac{dU}{dT} \cdot \frac{dT}{dt} \quad (4)$$

The entropic coefficient $\frac{dU}{dT}$ indicative of the thermodynamic potential change with temperature, reflects the intrinsic material properties and electrochemical kinetics under thermal modulation. This serves as the entropy variation for the entire cell and can be gauged by monitoring the shift in the OCV with respect to temperature.^[35–37] In our case, the term $\frac{dT}{dt}$ specifies the constant set rate of temperature change during a ramp. The factor $\frac{dQ}{dU}$ represents the capacity change concerning voltage, serves as a fundamental component when transferring from the OCV to the float experiment. From Equation (2), it becomes evident that I_E is directly proportional to the ramp speed $\frac{dT}{dt}$.

By incorporating Equations (2) into (4) and assuming constant ramp speed and $\frac{dQ}{dU}$ is constant over temperature for each examined float voltage, we derive:

$$I_E = \frac{dU}{dT} \cdot \frac{dT}{dt} \cdot \frac{dQ}{dU} = \pm \frac{d(A \cdot T + B \cdot T^2 + C)}{dT} \cdot \frac{dT}{dt} \cdot \frac{dQ}{dU} = \pm(A_{I_E} + B_{I_E} \cdot T) \quad (5)$$

The sign determination is based on I_E being positive or negative, while A_{I_E} is the offset value in A and B_{I_E} is the slope value in $\frac{A}{K}$. This formulation confirms the linearity of I_E as proven by Azzam et al.,^[33] supporting the applicability of our assumptions for both OCV and float current measurements in relation to temperature change.

Methodological Approach for the Validation of OCV as an Analog for Float Current

To convert the OCV over time into a physical quantity proportional to the float current, one must calculate the derivative of the voltage over time.^[27,28] The theoretical basis is predicated on:

$$\begin{aligned} I_{\text{self-discharge}} &= \frac{dU}{dt_{\text{OCV}}} \cdot \frac{dQ}{dU}(U_{\text{float}}) = \\ dQ/dt &= I_{\text{float}} \rightarrow I_{\text{float}} \propto \frac{dU}{dt_{\text{OCV}}} \end{aligned} \quad (6)$$

Similar to the float current I_{float} , the OCV change over time $\frac{dU}{dt_{\text{OCV}}}$, known as the voltage decay rate, comprises both, entropy-related and self-discharge-related voltage changes. Note that there is a sign inversion compared to the float current. A decreasing cell voltage (negative $\frac{dU}{dt}$) results in a positive current in the float current measurement, attempting to maintain a constant cell voltage and vice versa.^[38,39] The breakdown into the same two components as the float current results in:

$$\frac{dU}{dt_{\text{OCV}}} = \frac{dU}{dt_{\text{Aging}}} + \frac{dU}{dt_E} \quad (7)$$

The conversion factor from OCV to float current is the $\frac{dQ}{dU}(U_{\text{float}})$ as per Equation (6). To maintain consistency with DVA terminology and enhance the clarity of our analysis, we will refer to these measurements as $\frac{dQ}{dU}(U_{\text{float}})$. Therefore, we utilize temperature ramps with the same speed and direction to calculate $\frac{dU}{dQ}(U_{\text{float}}, T)$ by dividing float currents and voltage decay rates.

Methodological Approach for the Evaluation Methods of the Temperature Ramps

In our previous paper,^[33] we introduced two approaches for the evaluation of the float currents, which will also be applied for the voltage decay method. In a first approach, we utilize temperature ramp pairs to eliminate the entropy-induced measured current I_E . I_{Aging} is calculated as follows:

$$I_{\text{Aging}} = \frac{(I_{\text{float}\uparrow} + I_{\text{float}\downarrow})}{2} = \frac{(I_{\text{Aging}} + I_E\uparrow) + (I_{\text{Aging}} - I_E\downarrow)}{2} \quad (8)$$

With the help of this equation, we exclude the entropy effect and obtain the pure I_{Aging} within the temperature range. With the help of this method, the symmetry of float currents of upward and downward ramps can be assessed.

The same procedure is done for the OCV measurement, and the assumptions are also used for the voltage decay rate and results in:

$$\frac{dU}{dt_{\text{Aging}}} = \frac{\frac{dU}{dt_{\text{OCV}\uparrow}} + \frac{dU}{dt_{\text{OCV}\downarrow}}}{2} = \frac{\left(\frac{dU}{dt_{\text{Aging}}} + \frac{dU}{dt_E\uparrow}\right) + \left(\frac{dU}{dt_{\text{Aging}}} - \frac{dU}{dt_E\downarrow}\right)}{2} \quad (9)$$

A second evaluation method to obtain the aging current I_{Aging} from the ramp measurements involves different temperature ramp speeds, focusing exclusively on either the upward or the downward ramps. The I_{Aging} is calculated as follows:

$$\begin{aligned} I_{\text{Aging}} &= I_{\text{float}\uparrow}^{0.54\text{ K}} \cdot \left(1 - \frac{0.54\text{ K}}{0.54\text{ K} - 1.08\text{ K}}\right) + I_{\text{float}\uparrow}^{1.08\text{ K}} \cdot \\ &\quad \left(\frac{0.54\text{ K}}{0.54\text{ K} - 1.08\text{ K}}\right) \end{aligned} \quad (10)$$

Similarly, the analysis procedure utilized for float current measurement is applied to OCV measurements. For simplicity, we introduce the equivalent equation for the entropy-induced voltage decay rate in more detail as follows:

$$\frac{dU^{0.54\text{ K/h}}}{dt_{\text{OCV}\uparrow}} = \frac{dU}{dt_{\text{Aging}}} + \frac{dU^{0.54\text{ K/h}}}{dt_E\uparrow} \quad (11)$$

With $\frac{dU^{0.54\text{ K/h}}}{dt_E\uparrow}$ being equal to:

$$\frac{dU^{0.54\text{ K/h}}}{dt_E\uparrow} = \left(\frac{0.54\text{ K}}{0.54\text{ K} - 1.08\text{ K}}\right) \cdot \left(\frac{dU^{0.54\text{ K}}}{dt_{\text{OCV}\uparrow}} - \frac{dU^{1.08\text{ K}}}{dt_{\text{OCV}\uparrow}}\right) \quad (12)$$

With the help of Equations (11) and (12), we can calculate the resulting $\frac{dU}{dt_{\text{Aging}}}$ from two upward ramps with two different ramp speed. Analogously, this can be done for the downward ramps.

The separated aging part of the float current and the voltage decay rate of the temperature ramps is then compared to the steps profile for the validation of our analysis approach.

2. Results and Discussion

In the initial step of our analysis, we examine the raw data from both the float current and OCV measurements in detail. To maintain clarity and focus, we use the A123 cell at 3.2 V as a representative example. For readers interested in a broader dataset, comprehensive results for the remaining cells are provided in the Appendix A.1, with float current measurements displayed in Appendix Figure 1 of the Appendix A.1 and OCV measurements in.

The float measurement of the A123 at 3.2 V is depicted in Figure 4(a). In this scenario, the cell exhibits a negative entropy effect, where an increase in temperature leads to a decrease in voltage,^[40] and consequently, a higher float current I_{float} is observed (see Figure 4(c)). If the measured I_{float} turns out to be negative during a ramp, it indicates a positive entropy effect in the cell. Utilizing temperature ramps allows for the measurement of an entropy-induced current I_E along with the aging current I_{Aging} , unlike in temperature steps where only the steady-state current becomes visible after the entropy effect has subsided, as depicted in Figure 4(b). It is consistently found that a transient phase appears during any alteration in temperature. The nature of this transient current response is influenced by both, the rate of temperature change and the specific temperature range being changed. Moreover, a slight yet significant rise in the measured steady-state current is detected after each temperature increase. It is important to note that the measured values are presented as they are, without undergoing any filtering or adjustment. To address

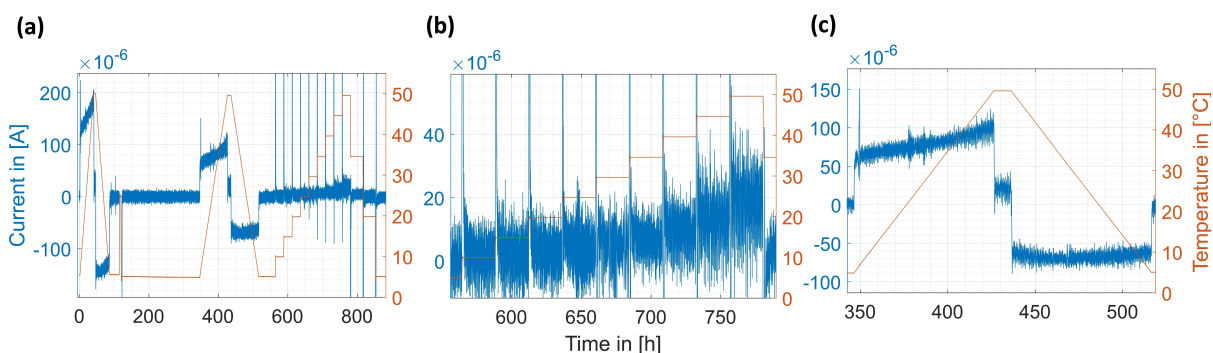


Figure 4. Measured current data I_{float} (blue) and temperature values (orange) for the A123 at 3.2 V in (a) full profile, (b) steps zoomed-in and (c) second ramp pair zoomed-in.

the noise observed in the float current measurements, a simple decimation filter is applied, averaging the data over 10 minutes intervals. This approach reduces noise while preserving the overall trends and allows for clear visualization of the data. Despite this, Figure 4 presents the unfiltered raw data, measured at one-second intervals, to demonstrate that even without filtering, the float current consistently exhibits temperature-dependent behavior. This highlights the reliability of the measurement methodology and the robustness of the observed trends.

Figure 5 demonstrates that the voltage measurement U_{OCV} for the A123 at 3.2 V is significantly clearer and the data acquisition, in comparison to the float current measurement, is much more distinct and less noisy. As outlined in section 2.2, the data from the U_{OCV} measurements will be differentiated with respect to time, allowing for a subsequent comparison and analysis between the float current I_{float} and the voltage decay rate $\frac{dU}{dt}_{\text{OCV}}$.

The subsequent sections will delve into the utilization of temperature ramps as a viable alternative methodology for conducting both OCV and float current measurements. In a last step, we will utilize the temperature steps as a reference method and then contrast these findings with the outcomes from the utilization of temperature ramps. This comparison will be conducted for both the OCV and float current measurements.

2.1. Measured Float Current and Voltage Decay Rate with Temperature Ramps

At first, we take a close look at the float current I_{float} measured during temperature ramps. Before separating the aging and entropy-induced currents, we will analyze the float current and voltage decay rate from OCV measurements obtained from the various ramps in the following subsections, focusing on the effects of ramp speed and analyzing the behavior shortly. In a first step, we compare the ramp speed for all cells to observe its effect on the measured float current I_{float} and the voltage decay rate $\frac{dU}{dt}_{\text{OCV}}$, starting off with the float current.

Figure 6 presents a filtered and decimated version of the float current measurements, where data was originally acquired in one-second intervals has been processed to represent averaged values over a 10 minute period. This filtering and decimation are applied to both the 0.54 K/h and 1.08 K/h ramp pairs across all tested cells and voltages. They are supported by polynomial curve fits further enhancing the visualization of observable trends. Now we are in the position to highlight the impact of ramp speed on the float current, offering a clear and concise depiction of our findings. For those interested in a more granular analysis or in validating our measurements, the original, unfiltered, and undecimated float current data is thoroughly documented in Appendix Figure 1 in Appendix A.1.

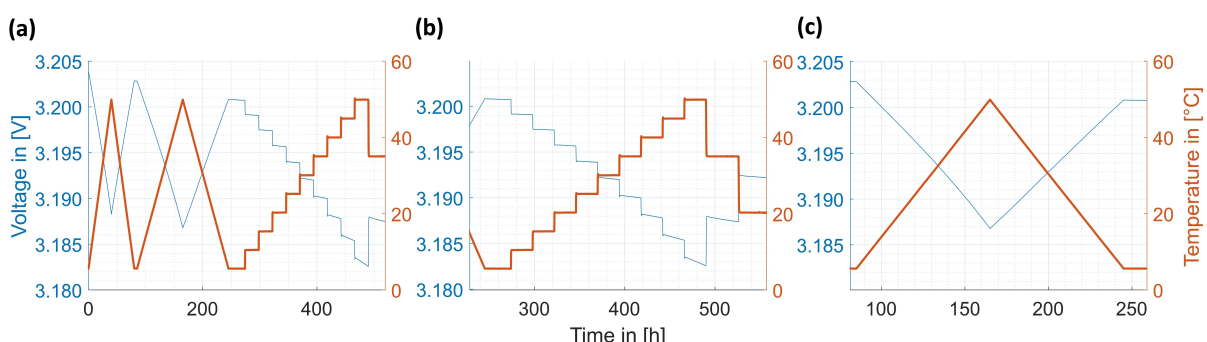


Figure 5. Measured voltage data U_{OCV} (blue) and temperature values (orange) for the A123 at 3.2 V in (a) full profile, (b) steps zoomed-in and (c) second ramp pair zoomed-in.

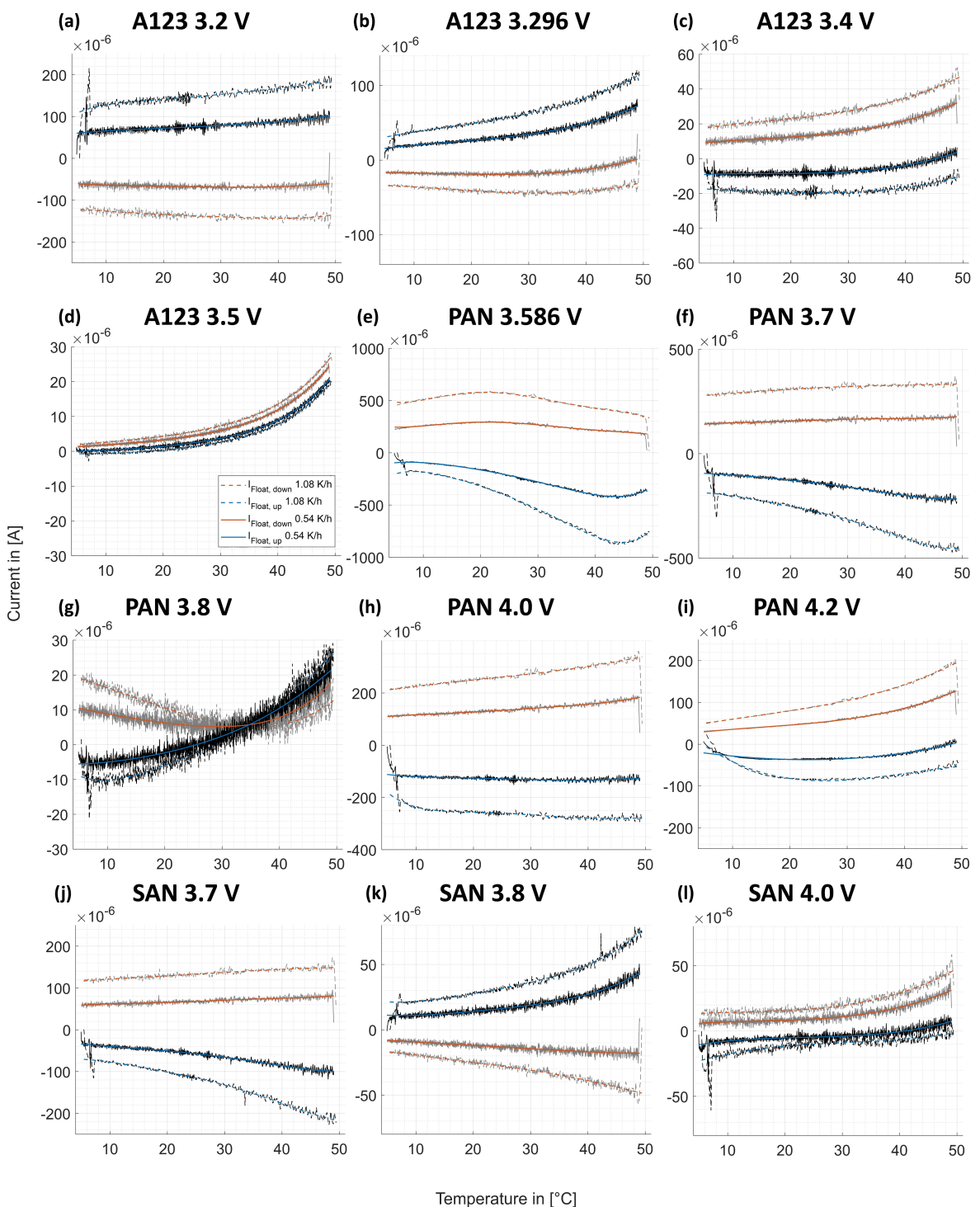


Figure 6. Measured decimated float current I_{float} for the A123 at (a) 3.2 V (b) 3.296 V, (c) 3.4 V and (d) 3.5 V, the PAN at (e) 3.586 V, (f) 3.7 V, (g) 3.8 V, (h) 4.0 V and (i) 4.2 V as well as the SAN at (j) 3.7 V, (k) 3.8 V and (l) 4.0 V for the ramp pair with a speed of 0.54 K/h and the ramp pair with a speed of 1.08 K/h. The blue fits represent those from the upward ramp, the orange ones from the downward ramp.

The Floater device allowed us to confirm the phenomena observed in previous studies^[33] with enhanced clarity, due to low noise current profiles. Specifically, we reobserved:

- **Consistent impact of ramp speed:** The consistency in the behavior of both upward and downward ramps with temper-

ature, showing a slight absolute increase in the distance between ramps at higher speeds.

- **Initial transient effects, entropy and temperature gradient caused compensation currents:** The recurrence of initial asymmetry due to internal cell gradients within the first 1–2 K of temperature change, necessitating the exclusion of

early upward and downward ramp results. The gradient-induced voltage differences, attributed to a combination of a temperature gradient and the entropy effect, are pronounced at lower start temperatures (around 5 °C), and diminish at higher temperatures starting at 20°C–30°C.

Moreover, our refined measurements have allowed for a better understanding of cell-specific behaviors without the interference of noise, notably:

- The A123 cells at 3.2 V demonstrate a notable entropy effect, with the 1.08 K/h ramp showing roughly double the float current compared to the 0.54 K/h ramp. However, at 3.5 V, this effect is minimal, resulting in similar float currents for both ramp speeds, as depicted in Figure 6 (d). This variance underscores the significant impact of entropy and ramp speed, particularly at 3.2 V. Similar patterns are observed for A123 cells at 3.296 V and 3.4 V, detailed in Figure 6 (b) and (c), with a more pronounced entropy effect at 3.296 V. A consistent observation across A123 cells is the symmetry in current profiles between upward and downward ramps, indicating valid measurements. At 3.4 V, however, the cell exhibits a positive entropy effect, unlike the three remaining cells, which display negative entropy effects as shown in Figure 6 (b).
- For PAN cells (Figure 6 (e) to (i)), we note a significant variability in entropy effect across voltages, with higher ramp speeds generally leading to increased currents. Specifically, at 3.7 V, 4.0 V, and 4.2 V, transient effects are more evident at higher ramp speeds. The most noticeable asymmetries are at 3.586 V, even at higher temperatures, highlighting the intricate relationship between entropy effect, ramp speed, and aging current. At 3.8 V, an asymmetry is observed, where the gap between ramp speeds widens slightly with temperature increases. This results in the crossing of the upward and downward measured float current.
- SAN cells at 3.7 V, 3.8 V, and 4.0 V (Figure 6 (j) to (l)) show a positive entropy effect at 3.7 V and 4.0 V, and a negative effect noted at 3.8 V. The significant asymmetries are at 3.7 V and 3.8 V, where the difference between lower and higher ramp speeds marginally increases with temperature, mirroring the behavior seen in PAN cells at 3.7 V.

In summary, the float current closely aligns with ramp speed and entropy coefficient. Notable transient effects at the start of upward ramps were seen in PAN cells. A123 cells displayed a consistent float current I_{float} pattern. Significant shape deviations between ramp speeds during upward ramps were evident in PAN cells at 3.586 V and 3.7 V, and SAN cells at 3.7 V and 3.8 V. The profiles of upward and downward ramps differ, with noticeable disparities in ramp speed distances, particularly in PAN and to some extent in SAN at 3.7 V. These differences can be attributed to the faster lateral balancing effects occurring at higher temperatures during upward ramps, compared to the slower effects observed at lower temperatures during downward ramps.^[33] The new insight for the PAN at 3.8 V was only possible due to the lower noise of the measurement compared to our previous publication.^[33]

In the following, we take a closer look at the OCV measurements. The primary focus is the analysis of the voltage decay rate $\frac{du}{dt}_{\text{OCV}}$ from the OCV measurements, aimed at evaluating the influence of variations in temperature and ramp speed. This analysis is showcased in Figure 7, for all cells and both ramp speeds providing a comprehensive view of the effects across the different conditions. The original OCV measurements, foundational for our analysis, are provided in Appendix A.1 in Appendix Figure 2.

When comparing the voltage decay rate $\frac{du}{dt}_{\text{OCV}}$ with float current I_{float} , we observe a corresponding inverse phenomenon, as anticipated when comparing the aging of the steps profile in 3.1. If the float current I_{float} exhibits a positive value in either the upward or downward ramp, the voltage decay rate $\frac{du}{dt}_{\text{OCV}}$ for the same ramp direction will manifest as negative, and vice versa. This consistent inverse relationship underscores the interplay between voltage decay and float current across temperature ramps, aligning with our expectations based on the cell's electrochemical behavior during aging.

As for the float currents, we monitor similar behavior, though with much less noise.

- **Ramp Speed Impact:** Both float currents and OCV measurements show an increased separation between upward and downward ramps at higher speeds, confirming the appropriateness of increased ramp speeds.
- **Initial Transient Effects:** The initial voltage decay in OCV measurements exhibits asymmetries within the first 1–2 K of temperature change, similar to float currents, necessitating the exclusion of early ramp data. These differences, driven by entropy effects, are more significant at lower temperatures (around 5 °C) and diminish above 50 °C.
- **Consistency in Curve Shapes:** OCV measurements, like float currents, display consistent curves between upward and downward ramps, indicating the robustness of our measurement techniques and the consistent, reversible response of electrochemical processes to temperature changes.

In the end, we see only two distinct cells that behave differently. In the OCV measurements, asymmetry was predominantly observed for PAN at 3.586 V, underscoring a specific electrochemical behavior at this voltage that implicates the interplay of entropy effects, ramp speed, and aging voltage decay rate. This matches what we obtained with our float current measurement. Additionally, the PAN cell at 3.8 V exhibits unusual voltage decay rate behavior starting at 35 °C across both ramp speeds and directions. Although asymmetrical, this behavior is consistent within its own patterns, differing from the OCV measurement trends, which will be demonstrated in the next section. These observations for the PAN cell at 3.8 V suggest an intricate and possibly anomalous behavior that warrants further investigation.

In summary, the analysis of voltage decay rates $\frac{du}{dt}_{\text{OCV}}$ from OCV measurements qualitatively complements our float current findings, presenting a consistent increase in separation between ramps at higher speeds, reaffirming the appropriateness of our methodology. Just like the float current, initial OCV results show asymmetry due to internal temperature gradients

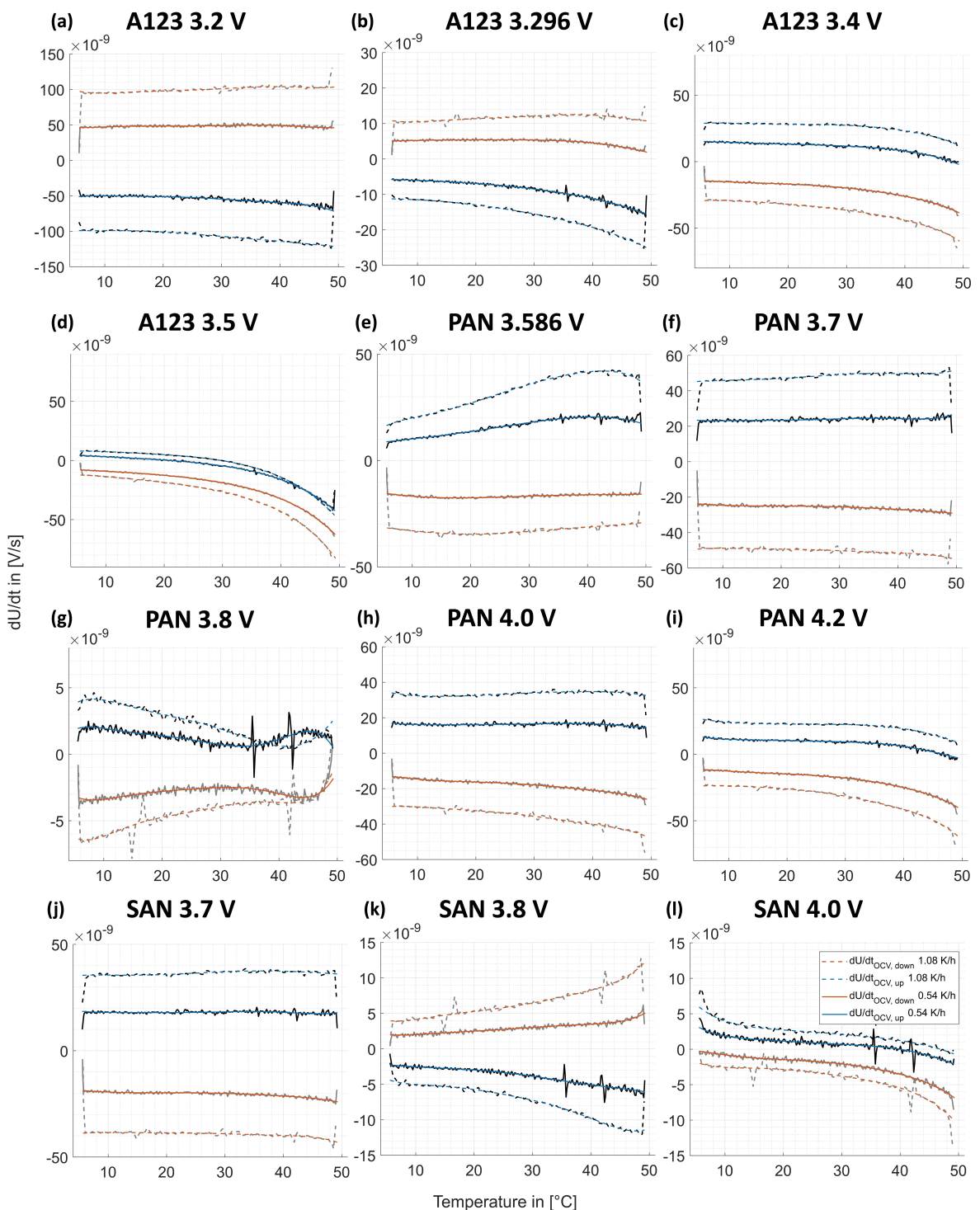


Figure 7. Measured voltage decay rate $\frac{dU}{dt_{OCV}}$ for the A123 at (a) 3.2 V (b) 3.296 V, (c) 3.4 V and (d) 3.5 V, the PAN at (e) 3.586 V, (f) 3.7 V, (g) 3.8 V, (h) 4.0 V and (i) 4.2 V as well as the SAN at (j) 3.7 V, (k) 3.8 V and (l) 4.0 V for the ramp pair with a speed of 0.54 K/h and the ramp pair with a speed of 1.08 K/h. The blue fits represent those from the upward ramp, the orange ones from the downward ramp.

in the cell, particularly noticeable within the first 1–2 K of temperature change, thereby necessitating the exclusion of early data. These entropy-driven voltage differences are most pronounced at lower temperatures, peaking around 5 °C, and become less significant as temperature approaches 50 °C, illustrating the temperature dependence of entropy on OCV.

For most cases, the OCV measurements also demonstrate symmetrical curves between upward and downward ramps, reinforcing the reliability of our measurement techniques. However, two cells exhibited distinct behavior: at 3.586 V, an asymmetry in OCV measurements suggests a complex interplay of factors, and the PAN cell at 3.8 V showed a peculiar

voltage decay rate behavior beginning at 35°C. While these behaviors remain consistent within their own patterns, they deviate from the general trends and signify unique electrochemical behaviors that may require further exploration to fully understand their implications. It must be noted that optical deviations between float and OCV measurements are not observed at the same voltage.

2.2. Comparison Between the Obtained Aging Current of the Ramps and Steps

In the following, the aging current measured during ramps and steps, will be compared. The goal of this comparison is to determine whether the continuous measurement approach used in ramps can capture aging dynamics with the same accuracy as the more traditional, discrete steps approach. By evaluating the consistency between these methods, we aim to assess whether ramps can serve as a faster and equally reliable alternative to steps for aging current measurements, while still accounting for the entropy effect. To eliminate the entropy effect in the ramps, we use two methods: the first matches upward and downward ramps with the same speed but opposing directions, and the second utilizes ramps with the same direction but different ramp speeds. For temperature steps, the entropy is excluded by waiting for the transient current to settle at each step. To obtain I_{Aging} from the steps profile, each temperature step is evaluated after 1 day, ensuring that the entropy-induced effect from the step becomes negligible. The measurements generally revealed a high degree of agreement between ramps and steps, though not universally. In the subsequent sections, we will delve deeper into each case. Here, both evaluation methods are applied. The first method relies on averaging the currents from temperature ramp pairs, aiming to cancel out the entropy-induced current I_E . The second method calculates I_{Aging} independently from upward and downward ramps at varying speeds to isolate the entropy's impact.

In our latest study, replicating the analysis of Azzam et al.,^[33] we obtained enhanced results and found a high level of consistency with our prior findings as can be seen in Figure 8.

In summary, 9 out of 12 cells displayed accordance in aging currents between ramps and steps using the first evaluation method, with all cells showing strong agreement using the second method. Notably, PAN cells at 3.586 V and 3.7 V, and the SAN cell at 3.7 V—comprising NMC or NCA chemistries—presented deviations at lower voltages. These cells, exhibiting a positive entropy effect, are of higher energy density compared to A123 cells. The observed discrepancies, particularly the asymmetry in I_{float} during temperature changes, hint at a common thermal response mechanism influenced by entropy due to temperature gradients. To quantify the effect of entropy on the SoC shift, we examined the entropy values of the cells showing discrepancies, focusing specifically on the impact of float currents. The mean entropy-induced current values are monitored over a 40 hour ramp.

The shift for the PAN cell at 3.586 V (500 μA mean value) is calculated as:

$$\text{SoC}_{\text{Shift}} = \frac{|I_E, \text{mean}|_{t_{\text{Ramp}}} \cdot t_{\text{Ramp}}}{C_N} = \frac{500 \mu\text{A} \cdot 40 \text{ h}}{3.2 \text{ Ah}} \approx 0.6 \% \quad (13)$$

For the PAN cell at 3.7 V (280 μA mean value) and the SAN cell at 3.7 V (125 μA mean value), the shifts are 0.3% and 0.3%, respectively. The A123 cell at 3.2 V, which is more consistent, serves as an exemplary validation, showing a shift of 0.3% with a mean value of 80 μA. These results highlight the broader applicability of this method across all cells.

This shift in SoC due to entropy-induced currents might explain why the first method does not always align well with the step measurements. The SoC shift affects the float point and its corresponding $\frac{dU}{dQ}$, leading to discrepancies between ramp and step evaluations.

The improved correlation in the latest measurements with the Floater in shape and magnitude, particularly notable with the second evaluation method, paves the way for a deeper understanding of the entropy effects driven by temperature gradients, warranting further investigation into their implications on cell aging and performance.

We now look at the aging voltage decay rate $\frac{dU}{dt_{\text{Aging}}}$ in Figure 9. The same analysis procedure for both ramps and steps utilized for float currents is used for the voltage decay. Here, we observe that all cells, apart from the PAN cells at 3.586 V and 3.8 V, each one behaving differently, demonstrate consistent patterns across both ramp and step measurements utilizing both evaluation methods.

Looking back at the voltage decay rate $\frac{dU}{dt_{\text{OCV}}}$ in Figure 7, it becomes clear that these two PAN cells, displaying unique asymmetries in their upward and downward ramps, are the same ones demonstrating discrepancies in the aging voltage decay rate. Specifically, the PAN cell at 3.586 V aligns closely with step measurements according to the second evaluation method, echoing its behavior in the float current analysis. For the PAN cell at 3.8 V, a strong correlation between steps and ramps persists up to 35°C using both evaluation methods. Beyond this temperature, however, neither method shows congruence between ramp and step data. This divergence, particularly noted in Figure 7 (j) for the upward and downward ramps of the PAN at 3.8 V, hints at a complex relationship between the cell's response to temperature changes and potentially entropy effects.

To further investigate the nuances observed in the aging voltage decay rate, particularly for the PAN cells at 3.586 V, 3.7 V and 3.8 V, as well as the SAN at 3.7 V, we will delve deeper into the analysis of entropy-induced current as well as the entropy's impact on the voltage decay rate. Detailed calculations and results are provided in Appendix A.2.

The difference between the voltage decay method and the float current method under temperature variation is mainly due to the entropy effect and $\frac{dU}{dQ}$ values. During floating, the entropy effect leads to a charge or discharge of the cell and affects the lithiation degree of anode and cathode changing $\frac{dU}{dQ}$ continuously. In case of a low absolute value of $\frac{dU}{dQ}$ combined

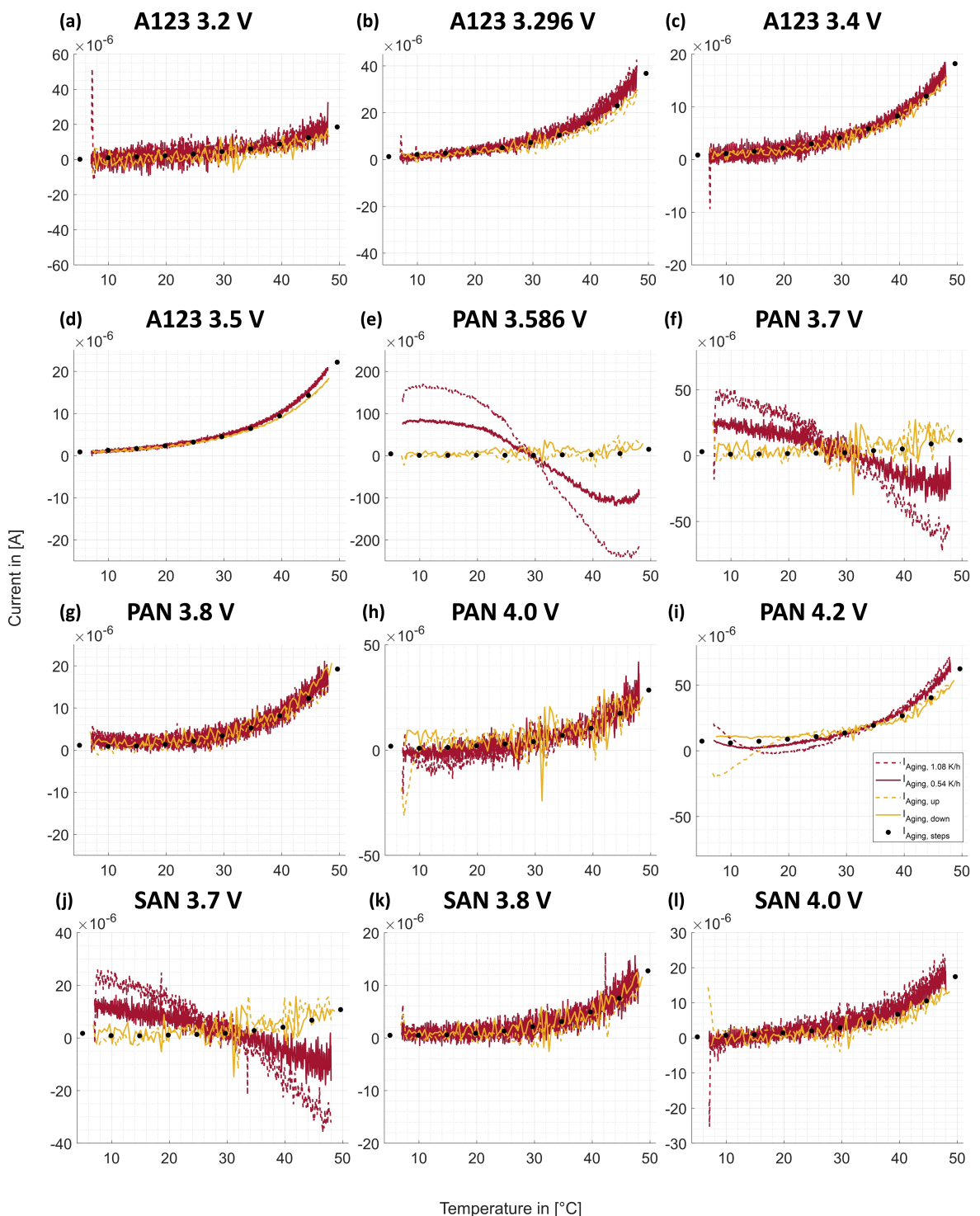


Figure 8. Calculated aging current I_{Aging} for the A123 at (a) 3.2 V (b) 3.296 V, (c) 3.4 V and (d) 3.5 V, the PAN at (e) 3.586 V, (f) 3.7 V, (g) 3.8 V, (h) 4.0 V and (i) 4.2 V as well as the SAN at (j) 3.7 V, (k) 3.8 V and (l) 4.0 V. The dark red lines are used for the first evaluation methods with the solid lines representing the speed of 0.54 K/h and the dashed lines representing the 1.08 K/h. The yellow lines are used for the second evaluation method with the dashed lines representing the upward ramps and the solid lines representing the downward ramps.

with a high entropy effect, this can have a significant impact on the measured float current leading to an inconsistent measurement. In comparison, the voltage decay method does not induce recharging due to the entropy effect or voltage

decay, as aging is negligible, given that the aging current is comparatively low at 30 °C.

A significant entropy effect is seen in the PAN cells at 3.586 V and 3.7 V. These cells show the highest entropy effects and the lowest aging rates, making float current measure-

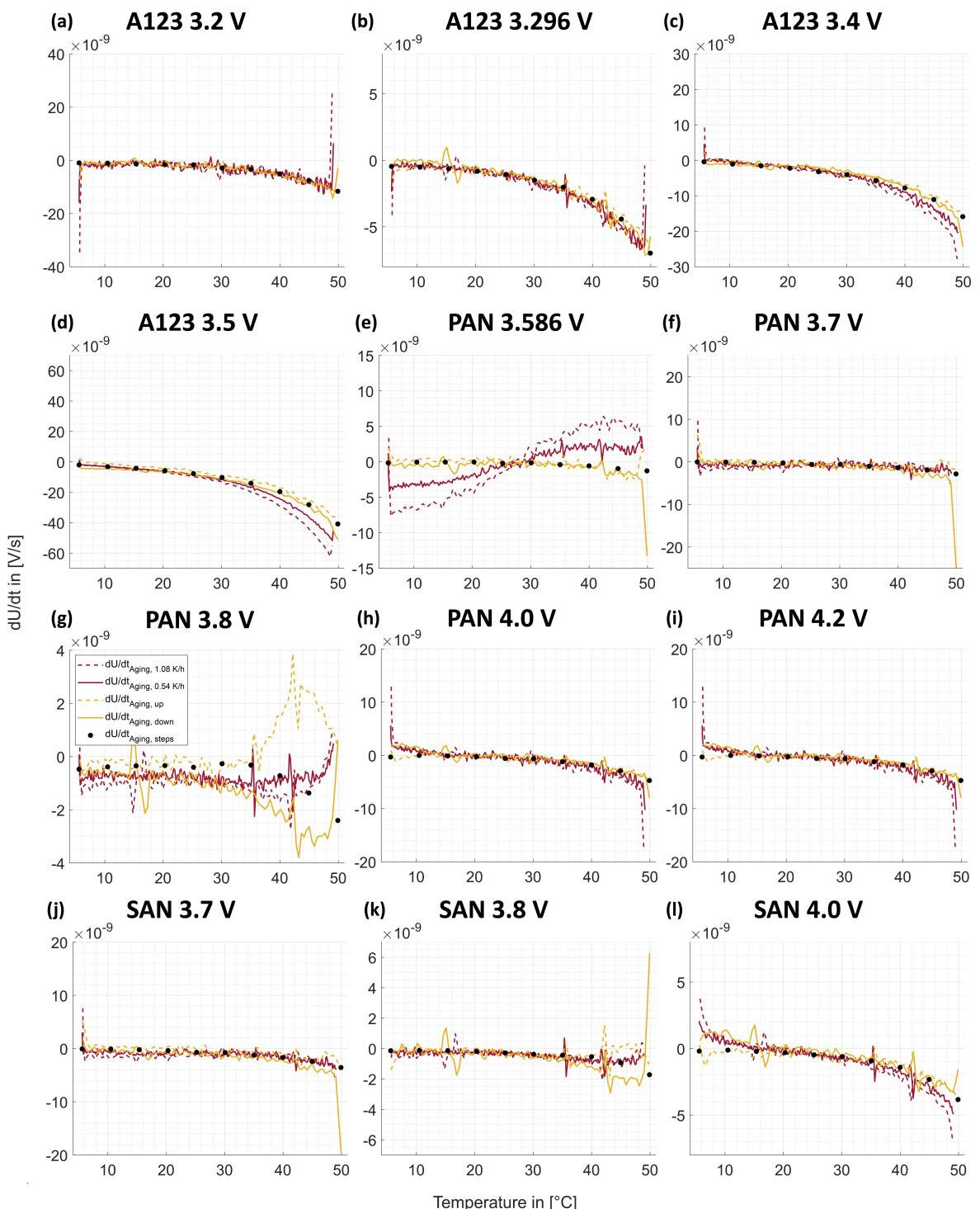


Figure 9. Calculated aging voltage decay rate $\frac{dU}{dt}_{\text{Aging}}$ for the A123 at (a) 3.2 V (b) 3.296 V, (c) 3.4 V and (d) 3.5 V, the PAN at (e) 3.586 V, (f) 3.7 V, (g) 3.8 V, (h) 4.0 V and (i) 4.2 V as well as the SAN at (j) 3.7 V, (k) 3.8 V and (l) 4.0 V. The dark red lines are used for the first evaluation methods with the solid lines representing the speed of 0.54 K/h and the dashed lines representing the 1.08 K/h. The yellow lines are used for the second evaluation method with the dashed lines representing the upward ramps and the solid lines representing the downward ramps.

ments problematic due to the strong entropy variations. The PAN cell at 3.8 V, although having similar $\frac{dU}{dQ}$ values as the 3.7 V PAN, has much less entropy effect, resulting in more stable float current measurements.

Similarly, the SAN cell at 3.7 V has the highest entropy effect and $\frac{dU}{dQ}$ values among SAN cells, causing significant issues with float current measurements due to high entropy-induced currents. These observations highlight the important role of

entropy in determining the accuracy and reliability of float current measurements, especially with temperature changes.

In the voltage decay method, the PAN cell at 3.586 V shows clear asymmetries observed in the upward and downward ramps due to high entropy values causing large compensation currents within the cell, especially with ramps starting at low temperatures. The PAN cell at 3.8 V shows a not yet explainable behavior as entropy is comparable low and cannot be clarified in this paper. For OCV the observed discrepancies are attributed to the voltage difference between the interior and exterior of the cells caused by the combination of temperature gradient and high entropy.

While OCV and float current measurements often align, discrepancies can arise. These differences are explainable through $\frac{dU}{dQ}$ values and entropy effects. Problems mainly occur when comparing upward and downward ramps, a challenge that can be mitigated in future tests by using method 2 instead of method 1. An exception is noted for PAN cells at 3.8 V, where unique behavior necessitates further investigation. These findings show how entropy and aging interact to affect the accuracy of different measurement methods under temperature changes.

To explore this interplay further, we now examine the $\frac{dU}{dQ}$ analysis to validate OCV as an analog for float current.

2.3. Validation of OCV as an Analog for Float Current via dU/dQ

For the validation of OCV as an analog for float current, we refer to section 2.2.1, specifically to Equations (5) and (6). These equations form the foundation for our validation. The evaluation method focused solely on entropy is designated as method 1 and is used mainly in the manuscript, as it avoids singularities. This method ensures a nearly constant current, which is ideal for accurate analysis. In contrast, the evaluation method that includes the full measured current and voltage decay rate is labeled as method 2. Since the full measured

currents and voltages do not provide additional value to the main analysis, they are detailed in Appendix A.3 for completeness. This separation ensures clarity and focuses on the most relevant data for the manuscript. [Q1]

In total two $\frac{dU}{dQ}$ determination methods are used and compared. The first method uses the DVA via the Galvanostatic Intermittent Titration Technique (GITT).^[41] In GITT, the battery is subjected to a series of current pulses followed by relaxation periods where no current is applied. During these relaxation periods, the voltage stabilizes, allowing for accurate OCV measurements as can be seen in Figure 10 (a) for the SAN cell. With that we obtain a DVA curve resembling the quasi-OCV behavior of the cell, and we can obtain the $\frac{dU}{dQ}_{\text{GITT}}$. The second method is the $\frac{dU}{dQ_{\text{Pulse}}}$ pulse measurement, involving the application of minor current pulses at a predetermined float voltage to precisely measure the differential voltage change in relation to charge. This is done after all transient effects, particularly the anode overhang, have concluded.^[6] An example is given in Figure 10 (b). The execution of $\frac{dU}{dQ_{\text{Pulse}}}$ measurements is conducted using a dual-method approach to affirm the robustness. The initial stage involves setting the target float voltage via a current rate pulse of $\frac{C}{1000}$. To compute $\frac{dU}{dQ_{\text{Pulse}}}$, we record the final voltage and the corresponding change in charge (ΔQ) during the current pulse.

This methodology is executed through two approaches, denoted as 'hold' and 'ramp', illustrated in green and red, respectively. The procedure, shown in Figure 10, for the SAN at 4.0 V commences with a minimal cell discharge using a current rate of $\frac{C}{1000}$ for an hour, followed by a waiting period of 2 hours to allow the voltage to stabilize, equivalent to a DoD of 0.1%. Subsequently, the cell is charged with the same current for 2 hours, which is twice the initial discharge duration. After charging, the same hold period of 2 hours is executed. The $\frac{dU}{dQ_{\text{Pulse}}, \text{Hold}}$ measurement is captured between the green lines indicating stabilization, whereas the $\frac{dU}{dQ_{\text{Pulse}}, \text{Ramp}}$ measurement occurs during the second, doubled charging period as it intersects the float voltage point. This procedure was applied across 12 cells at three temperature points: 5 °C,

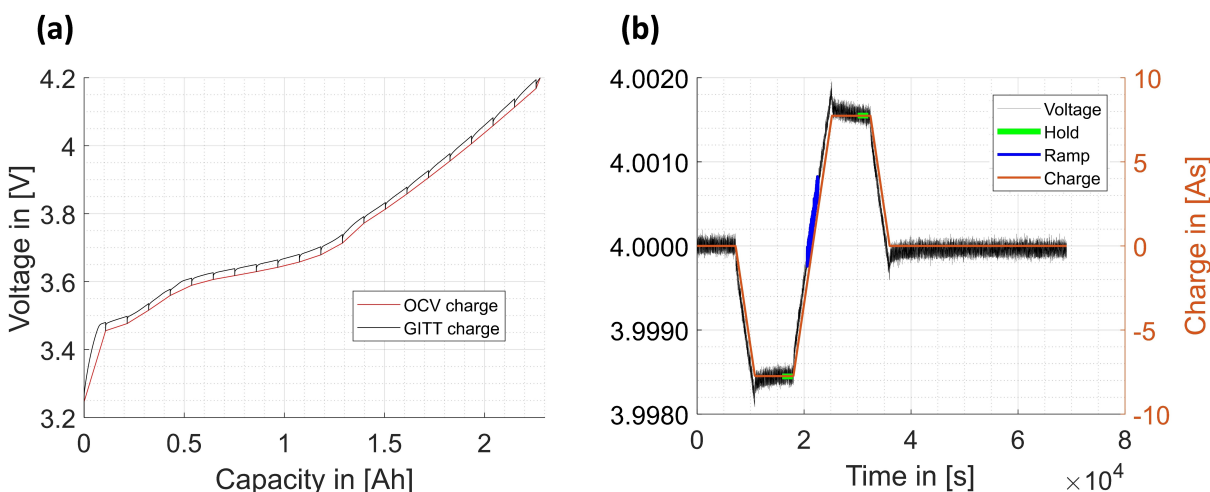


Figure 10. (a) Measured GITT for the SAN cell (b) Measured voltage data (blue) and charge (orange) during the $\frac{dU}{dQ_{\text{Pulse}}}$ measurement of the SAN at 4.0 V at 25 °C utilizing hold (green lines) and ramp (blue line) methodologies.

25 °C, and 50 °C, to evaluate the temperature's influence on $\frac{dU}{dQ_{Pulse}}$.

In Figure 11, the comparison between the GITT DVA and $\frac{dU}{dQ_{Pulse}}$ methods is visualized for the three cells at 25 °C. A commonality between all cells is that the $\frac{dU}{dQ_{Pulse}}$ exhibits a lower negative value corresponding to a higher slope at each measured point when compared to the $\frac{dU}{dQ_{GITT}}$.

The $\frac{dU}{dQ}$ results utilizing the entropy measurements of the 12 cells along with their $\frac{dU}{dQ_{Pulse}}$ of the hold and ramp are plotted in Figure 12. Our analysis indicated that both $\frac{dU}{dQ_{Pulse, Hold}}$ and $\frac{dU}{dQ_{Pulse, Ramp}}$ methods yielded consistent results, with an exception for the PAN at 4.2 V, which exhibited a transient effect at lower temperatures in Figure 12, confirming the repeatability and reliability of the measurements.

Consistency of $\frac{dU}{dQ_E}$ with $\frac{dU}{dQ_{Pulse}}$ measurements is observed across SAN, A123, and PAN cells, particularly when no zero crossing occurs, as exemplified by the A123 at 3.5 V, solely for the downward ramp case, and the PAN at 3.8 V. It is crucial to note that all $\frac{dU}{dQ_{Pulse}}$ values increase with temperature. This highlights a fundamental characteristic of $\frac{dU}{dQ_{Pulse}}$ values, accentuating their susceptibility to temperature variations and rising with temperature increment. It is noteworthy that these $\frac{dU}{dQ_{Pulse}}$ values consistently have a larger absolute value than those obtained via GITT measurements, with differences ranging between a factor of two to five times the magnitude. This along with the temperature sensibility was also validated by Streck et. al.^[23] while measuring the Incremental capacity analysis (ICA) at different temperatures. The incorporation of entropy into the analysis results in a measurement trajectory that the model captures more accurately, with a linear relationship in the current and a quadratic relationship in the OCV.

However, the PAN cell at 3.8 V presents an anomaly. It shows an atypical entropy-induced current I_E , with a positive offset and negative slope during downward temperature ramps, and a negative offset and positive slope during upward ramps, indicating a complex response to temperature changes. As discussed in previous chapters, this cell maintains a strong correlation between steps and ramps up to 35 °C for the voltage decay aging as highlighted in Figure 9(j). Beyond this temperature, however, both evaluation methods did not show congruence. This divergence underscores the unique and erratic behavior of the PAN cell at 3.8 V.

This analysis highlights key differences between the OCV and float current measurement techniques. During OCV measurements, even without active current, small voltage changes in the millivolt range occur, indicating a slight drift in the OCV measurement point. Both downward and upward ramps are assumed to cause similar entropy effects, consistently aiming for the same target voltage. However, aging causes a very slight change in the achieved voltage. In the float current measurements, the voltage remains constant, causing a slight shift in the delithiation points. Assuming similar conditions as in the OCV measurements, the starting point remains mostly unchanged, but aging introduces a small variation towards lower voltages. When these voltage points are examined on the anode curve, both parameters consistently appear on the second flat region. This consistency may indicate a critical factor in understanding the direction of changes in the $\frac{dU}{dQ}$. The second evaluation method utilizing the full measurements and calculating $\frac{dU}{dQ_{Full}}$ is found in Appendix A.3. In general, the same conclusion is reached utilizing both evaluation methods.

For a more comprehensive analysis about the possible reasons for the deviation between $\frac{dU}{dQ_{Pulse}}$ and $\frac{dU}{dQ_{GITT}}$, we take a closer look at the factors that play an important role in the determination of $\frac{dU}{dQ}$. The factors are the temperature, SoC, C-rate and lastly the DoD. Assuming we measure the $\frac{dU}{dQ}$ at the same SoC and holding the temperature constant, we analyse the two remaining effects, the C-rates and DoD.

As the cells were still under test, we used another cell type also with pure graphite on the anode to illustrate the principle of this hysteresis effect of the graphite. Explicitly we tested four 2900 mAh Samsung INR18650 29 E cells, labeled as Cell 33, 34, 35, and 40, all charged to 3.6 V and with a state of health of 90%. In Figure 13(c), the GITT DVA of the four cells is shown. All cells behave similarly and, the $\frac{dU}{dQ_{GITT}}$ at 3.6 V is approximately -0.23 V/Ah. In the first step, we measured the $\frac{dU}{dQ_{Pulse}}$ for all four cells with varying C-rates from $\frac{C}{1000}$ to $\frac{C}{10}$ logarithmically spaced, and a constant DoD of 0.1%. The results are shown in Figure 13(a), where the almost identical behavior of all four cells is evident, with $\frac{dU}{dQ_{Pulse}}$ values of -0.45 V/Ah, almost twice as high as $\frac{dU}{dQ_{GITT}}$. This indicates that the decisive factor is the DoD. Therefore, we conducted a second test procedure, where a varying logarithmically spaced DoD between 0.1% and 10% is utilized. For the first range

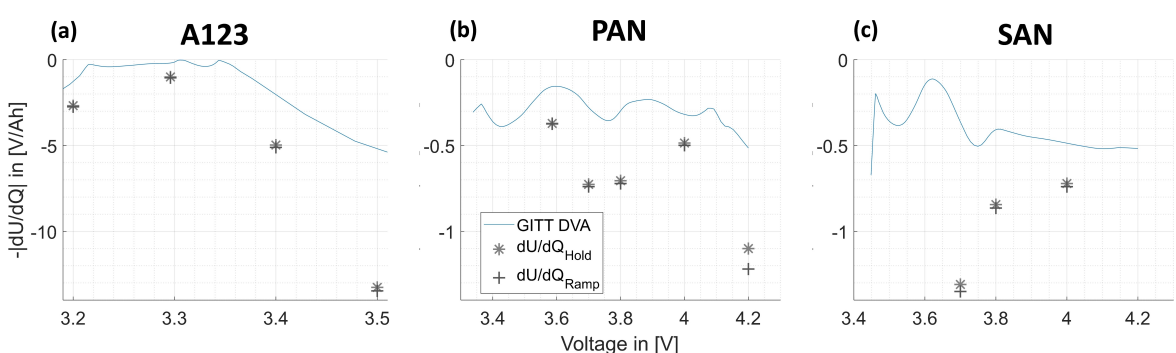


Figure 11. Comparison between the obtained GITT DVA at 30 °C and the measured $\frac{dU}{dQ_{Pulse, Hold}}$ and $\frac{dU}{dQ_{Pulse, Ramp}}$ at 25 °C for the (a) A123, (b) PAN and (c) SAN.

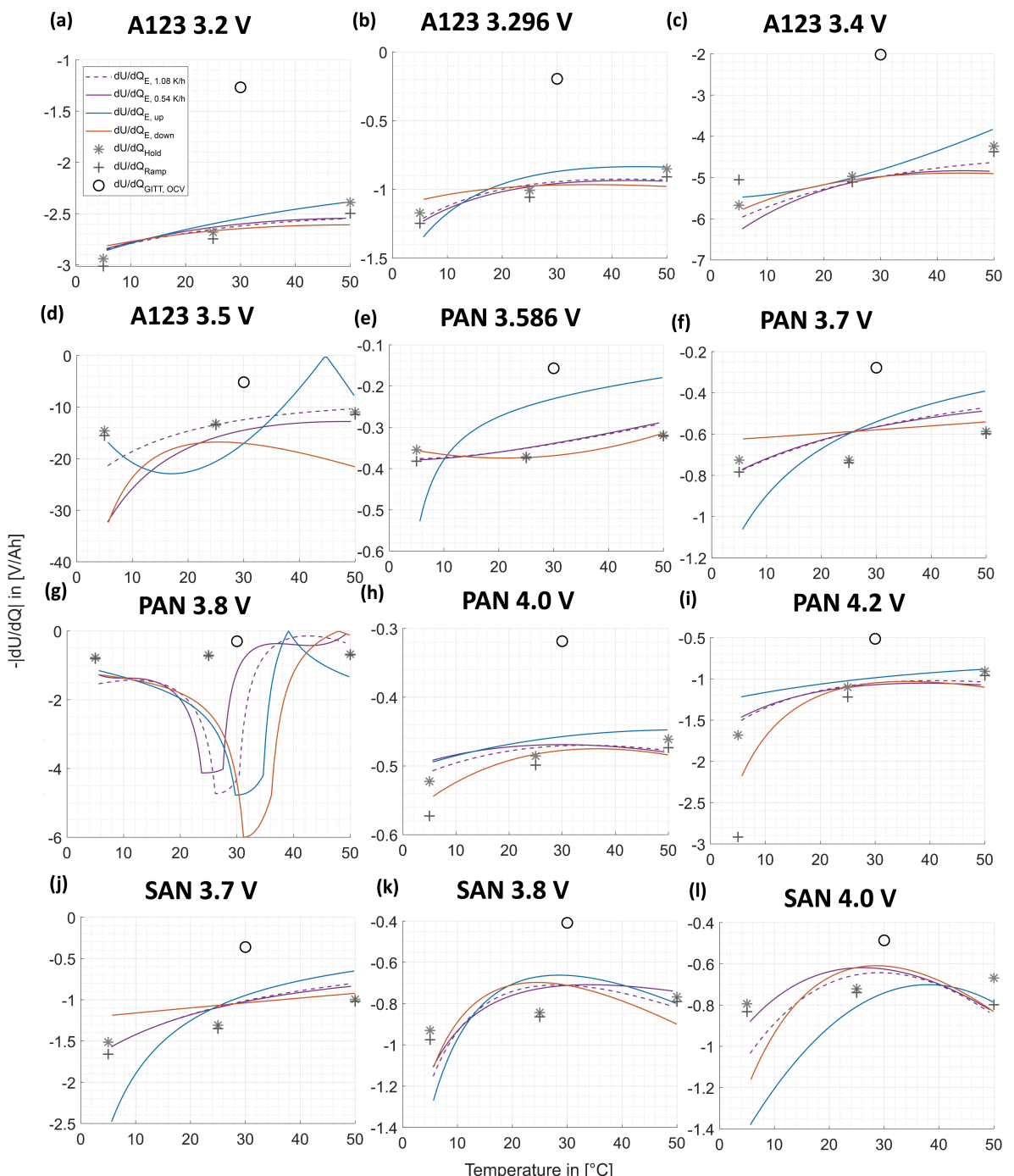


Figure 12. $\frac{dU}{dQ}$ for the A123 at (a) 3.2 V (b) 3.296 V, (c) 3.4 V and (d) 3.5 V, the PAN at (e) 3.586 V, (f) 3.7 V, (g) 3.8 V, (h) 4.0 V and (i) 4.2 V as well as the SAN at (j) 3.7 V, (k) 3.8 V and (l) 4.0 V. For the ramp pair with a speed of 0.54 K/h (solid lines) and the ramp pair with a speed of 1.08 K/h (dot-dashed lines) the results are plotted in purple utilizing the first evaluation method of the entropy. Using the second evaluation method for the entropy the results for the downward ramps are plotted in red solid lines and for the upward ramps are blue solid lines. The plus represents the $\frac{dU}{dQ}_{\text{Pulse}, \text{Hold}}$, the asterisk represents the $\frac{dU}{dQ}_{\text{Pulse}, \text{Ramp}}$ and the black circle represents the $\frac{dU}{dQ}_{\text{GITT}}$.

between 0.1% and 1% a C-rate of $\frac{C}{100}$ is used, and for the range between 1% and 10% a C-rate of $\frac{C}{10}$ is used. The results are plotted in Figure 13(b), where it becomes clear that with a higher DoD, a steeper $\frac{dU}{dQ}$ is calculated, corresponding to $\frac{dU}{dQ}_{\text{pulse}}$. The slope then decreases with decreasing DoD, forming an S-curve shape. When reaching a DoD of 5%, the $\frac{dU}{dQ}$ becomes

almost constant and reaches a value equivalent to that of $\frac{dU}{dQ}_{\text{GITT}}$.

For float current and voltage decay experiments, pulses are more suitable than GITT values.

Pulse measurements were found to provide higher consistency and accuracy compared to GITT for $\frac{dU}{dQ}_{\text{GITT}}$ evaluation. While GITT measurements are influenced by graphite hysteresis,

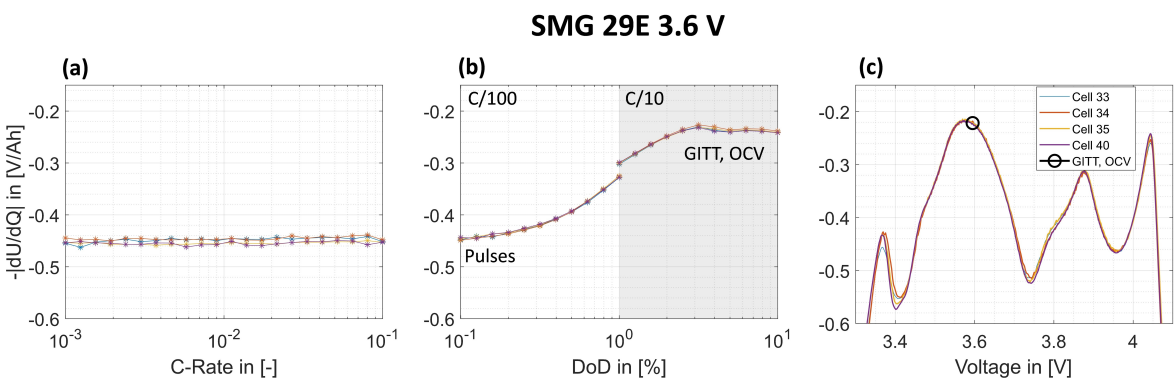


Figure 13. $\frac{dU}{dQ}$ measurements for four Samsung INR18650 29 E cells at 3.6 V with 90% state of health. (a) $\frac{dU}{dQ_{\text{Pulse}}}$ values measured with varying C-rates from C/1000 to C/10 and a constant DoD of 0.1%, (b) $\frac{dU}{dQ_{\text{Pulse}}}$ values measured with varying DoD between 0.1% and 10%, highlighting a steeper (c) $\frac{dU}{dQ_{\text{GITT}}}$ GITT DVA results for the four cells.

resis and show significant variability at low DoD, pulse-based $\frac{dU}{dQ_{\text{Pulse}}}$ values exhibit smoother trends and better reproducibility. This aligns with findings in recent literature, which highlight the limitations of GITT under certain conditions.^[42] By mitigating non-linearities, pulse measurements offer a reliable basis for linking voltage decay rates to float current behavior.

Converting $\frac{dU}{dQ}$ values from pulses to GITT reveals that the values depend solely on DoD, independent of the current rate. This clear transfer with increasing DoD may indicate hysteresis effects resulting from the nature of graphite.^[43–45]

In summary, GITT DVA is not returning suitable results for voltage decay and float current experiments. Instead pulse DVA fits significantly better. However, we highlighted that using the right DOD is necessary to find the appropriate dU/dQ value, showing the problems arising evaluating voltage decay instead of float currents.

2.4. Aging Current and Voltage Decay Rate Measured with Temperature Steps

In this section we take a close look at the measured float current, I_{float} during temperature steps. Results for I_{Aging} are depicted in Figure 14 (a) for A123, (b) for PAN, and (c) for SAN.

The aging current increases with rising cell temperatures following an exponential relation as reported by Theiler et al., Lewerenz et al. and Azzam et al.^[19,20,33] To visualize the exponential nature of I_{Aging} , an exponential fit is applied to the measured steps and plotted within the same figure:

$$I_{\text{Aging Model}} = a \cdot \exp^{(b \cdot T)} \quad (14)$$

Deviations are primarily observed at lower temperatures, around 5 °C, where the aging current is very small and the impact of charge redistribution due to the entropy effect and low ionic conductivity become visible.

As the float currents originate from anodic and cathodic aging effects (Azzam et al.^[21]), they increase non uniformly with the test voltage. This is visible particularly for A123 as here the voltage dynamic of the cathode is remarkably high.

In Figure 14(d-f), we illustrate the observed $\frac{dU}{dQ_{\text{Aging}}}$ from the step profile analysis of the voltage decay experiment. Notably, at 5 °C, the instability of the values is particularly pronounced for the SAN cell, diverging from the otherwise consistent trend of an increase in $\frac{dU}{dQ_{\text{Aging}}}$ across temperatures. With the help of Equations (6) and (13), we can deduce the following fit function for $\frac{dU}{dQ_{\text{Aging}}}$:

$$\frac{dU}{dQ_{\text{Aging Model}}} = -d \cdot \exp^{(b \cdot T)} \quad (15)$$

With d additionally comprising the $\frac{dU}{dQ}$ value at the specific test voltage. Due to strong variations in $\frac{dU}{dQ}$ and the test voltage, the sorting according to the float voltages is diverging especially for A123 (see Figure 14 (a) and (d)). The negative sign reflects the inverse relationship between the direction of voltage change and the induced float currents as the aging induced voltage decay must be recharged with a positive current.

A third and final validation for the analogy of OCV and float currents was performed using the measured steps. Initially, we fit a first-degree spline to the measured points of $\frac{dU}{dQ_{\text{Pulse}}}$ for three different temperatures as can be seen in Figure 14 (a-c). Subsequently, we take the measured $\frac{dU}{dQ_{\text{Aging}}}$ from the steps profile and divide it by the fit of $\frac{dU}{dQ_{\text{Pulse}}}$. The results of the estimated I_{Aging} from the voltage decay rate and $\frac{dU}{dQ_{\text{Pulse}}}$ are given in Figure 14 (g-i).

Comparing the obtained I_{Aging} from the $\frac{dU}{dQ_{\text{Pulse}}}$ fit and $\frac{dU}{dQ_{\text{Aging}}}$ with the measured data in Figure 14, the SAN cell is the most consistent transferring voltage decay into float currents. For the A123 cell at 3.296 V, it remains the highest in aging current, although with a lower current at 50 °C. Another notable divergence is observed at 3.5 V, which becomes the lowest in current. Examining the PAN cell at 4.2 V, it continues to show the highest aging current, but with a higher value at 50 °C. However, for the PAN cell at 3.8 V, it shifts to the lowest current, whereas it was the third highest in the measured aging current. These discrepancies underscore the complexity of analyzing OCV measurements as the $\frac{dU}{dQ_{\text{Pulse}}}$ must be precisely known for the temperature and voltage range combined with

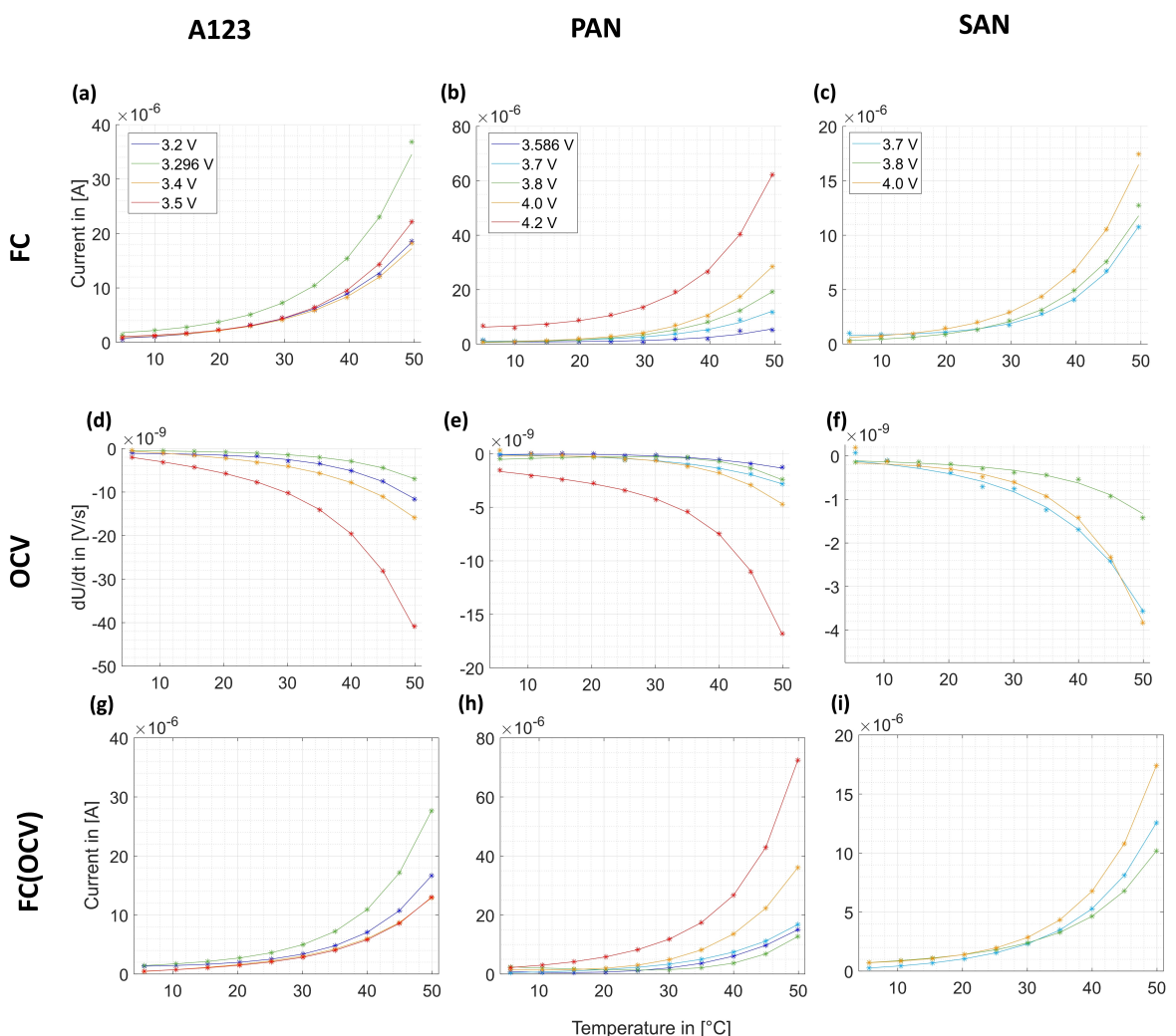


Figure 14. Measured aging current I_{Aging} for the (a) A123, (b) PAN and (c) SAN for all cell voltages for the steps profile (stars) and a simple exponential fit for the measured aging current (line). Measured aging voltage decay rate $\frac{dU}{dt}_{\text{Aging}}$ for the (d) A123, (e) PAN and (f) SAN for all cell voltages for the steps profile (stars) and a simple exponential fit for the measured voltage over time derivative (line). Calculated aging current I_{Aging} for the (g) A123, (h) PAN and (i) SAN for all cell voltages for the steps profile based on the $\frac{dU}{d\text{Opulse}}$ spline fit and $\frac{dU}{dt}_{\text{Aging}}$.

the DOD during measurement including aging-induced effects. This indicates the challenges and intricacies involved in OCV analysis, highlighting the advantages of float current measurements for evaluating cell aging and performance.

3. Conclusions

In this study, we investigated the behavior of three types of lithium-ion cells with varying cathode active material under thermal stress by comparing OCV analysis with float current measurements. For both strategies we included a long constant voltage phase to compensate transient effects stemming mainly from the anode overhang effect. Utilizing our state-of-the-art, self-developed Floater system, we have achieved a more pronounced measurement by reducing measurement noise and filtering compared to previous studies and demonstrated the relationship between entropy effects, cell aging, and temperature variations at even lower currents.

Our dual-method approach reaffirms that both, OCV with $\frac{dU}{dt}$ and float current measurements I_{float} , yield similar results indicating that float currents essentially recharge the OCV without triggering additional unwanted aging mechanisms. This highlights the importance of a longer constant voltage phase before the test to assure same test voltages regarding aging. Before conducting any tests, the cells should be held at the desired voltage until the float current stabilizes below $50 \mu\text{A}$ for 18650 cells at 30°C , ensuring that transient effects such as polarization and anode overhang have subsided. This allows for subsequent measurements to accurately reflect the aging dynamics, free from initial stabilization effects.

In the next step, we investigated how the relationship between float current and OCV measurements varies across different temperature ramps and steps, comparing ramp pairs in terms of direction and speed. While OCV measurements do not recharge voltage decay due to aging, float measurements recharge entropy effects causing differences among both test strategies in some dynamic tests. Assuming aging as the root

cause for float currents and voltage decay, one must convert voltage decay into an aging current. Despite, being technically easier and producing less measurement noise, OCV measurements must be converted by the factor $\frac{dU}{dQ}$ which has strong and complex dependencies on several parameters as temperature, SoC, aging, and DoD. A significant observation is the temperature-dependent increase in $\frac{dU}{dQ_{\text{Pulse}}}$ values, which always show a steeper slope than those from GITT measurements, fits best to conversion of OCV into float currents. The Floater system enhances battery diagnostics through float current measurements compared to the more labor-intensive OCV and $\frac{dU}{dQ_{\text{Pulse}}}$ approaches by requiring less after processing.

Finally, using float current analysis with high quality measurement as we demonstrated here and OCV approach will improve current modelling by more precise temperature dependence of aging, entropy, heat flow, anomalies, and the dependencies of DVA in such an experiment.

Acknowledgements

The research is funded by two projects. 1.) Grant number: 440701024 funded by German Research Foundation (DFG); 2.) Grant number: 03XP0442 funded by German Federal Ministry of Education and Research (BMBF). Special thanks for the fruitful discussion and support to Qing Yu, Iqra Kiran, and Simon Diehl. Open Access funding enabled and organized by Projekt DEAL.

Conflict of Interests

The authors declare no conflict of interest.

Keywords: 18650 · NCA · NMC · LFP · Graphite · Float current analysis · Potentiostatic hold · Self-discharge rate · Modelling · Temperature · Thermodynamics · Entropy · OCV · Pulse measurement · Voltage decay

- [1] M. A. Danzer, V. Liebau, F. Maglia, *Advances in Battery Technologies for Electric Vehicles* (Eds: B. Scrosati, J. Garche, W. Tillmetz), Elsevier Science, Burlington 2015, 359–387.
- [2] E. Redondo-Iglesias, P. Venet, S. Pelissier, *Batteries* 2020, 6, 14. <https://doi.org/10.3390/batteries6010014>.
- [3] S. Paarmann, M. Schreiber, A. Chahbaz, F. Hildenbrand, G. Stahl, M. Rogge, P. Dechent, O. Queisser, S. D. Frankl, P. Morales Torricos, Y. Lu, N. I. Nikolov, M. Kateri, D. U. Sauer, M. A. Danzer, T. Wetzel, C. Endisch, M. Lienkamp, A. Jossen, M. Lewerenz, *Batteries & Supercaps* 2024. <https://doi.org/10.1002/batt.202300594>.
- [4] M. Ecker, N. Nieto, S. Käbitz, J. Schmalstieg, H. Blanke, A. Warnecke, D. U. Sauer, *Electrochim. Solid-State Lett.* 2014, 248, 839–851. <https://doi.org/10.1016/j.jpowsour.2013.09.143>.
- [5] S. Grolleau, I. Baghdadi, P. Gyan, M. Ben-Marzouk, F. Duclaud, *WEV* 2016, 8, 339–349. <https://doi.org/10.3390/wev8020339>.
- [6] M. Azzam, R. Scheuer, C. Endisch, M. Lewerenz, *Energies* 2023, 16, 3889.
- [7] M. Lewerenz, J. Münnix, J. Schmalstieg, S. Käbitz, M. Knips, D. U. Sauer, *J. Power Sources* 2017, 345, 254–263. <https://doi.org/10.1016/j.jpowsour.2017.01.133>.
- [8] M. Lewerenz, G. Fuchs, L. Becker, D. U. Sauer, *J. Storage Mater.* 2018, 18, 149–159. <https://doi.org/10.1016/j.est.2018.04.029>.
- [9] T. Roth, L. Streck, A. Graule, P. Niehoff, A. Jossen, *J. Electrochim. Soc.* 2023, 170, 20502. <https://doi.org/10.1149/1945-7111/acb669>.
- [10] F. Hildenbrand, D. Ditscheid, E. Barbers, D. U. Sauer, *App. Energy* 2023, 332, 120395. <https://doi.org/10.1016/j.apenergy.2022.120395>.
- [11] S. Käbitz, J. B. Gerschler, M. Ecker, Y. Yurdagel, B. Emmermacher, D. André, T. Mitsch, D. U. Sauer, *J. Power Sources* 2013, 239, 572–583. <https://doi.org/10.1016/j.jpowsour.2013.03.045>.
- [12] P. Keil, S. F. Schuter, J. Wilhelm, J. Travi, A. Hauser, R. C. Katl, A. Jossen, *J. Electrochim. Soc.* 2016, A1872–A1880.. <https://doi.org/10.1149/2.0411609jes>.
- [13] D. Li, D. L. Danilov, L. Gao, Y. Yang, P. H. L. Notten, *J. Electrochim. Soc.* 2016, 163, A3016–A3021. <https://doi.org/10.1149/2.0821614jes>.
- [14] J. Belt, V. Utgikar, I. Bloom, *J. Power Sources* 2011, 196, 10213–10221. <https://doi.org/10.1016/j.jpowsour.2011.08.067>.
- [15] S. K. Rechekemmer, X. Zang, W. Zhang, O. Sawodny, *J. Storage Mater.* 2020, 30, 101547. <https://doi.org/10.1016/j.est.2020.101547>.
- [16] J. de Hoog, J.-M. Timmermans, D. Ioan-Stroe, M. Swierczynski, J. Jaguemont, S. Goutam, N. Omar, J. van Mierlo, P. van den Bossche, *Appl. Energy* 2017, 200, 47–61. <https://doi.org/10.1016/j.apenergy.2017.05.018>.
- [17] B. Epding, B. Rumberg, H. Jahnke, I. Stradtmann, A. Kwade, *J. Storage Mater.* 2019, 22, 249–256. <https://doi.org/10.1016/j.est.2019.02.015>.
- [18] N. Bouchhima, M. Gossen, S. Schulte, K. P. Birke, *J. Storage Mater.* 2018, 15, 400–407. <https://doi.org/10.1016/j.est.2017.11.014>.
- [19] M. Lewerenz, S. Käbitz, M. Knips, J. Münnix, J. Schmalstieg, A. Warnecke, D. U. Sauer, *J. Power Sources* 2017, 353, 144–151. <https://doi.org/10.1016/j.jpowsour.2017.03.136>.
- [20] M. Theiler, C. Endisch, M. Lewerenz, *Batteries* 2021, 7(22). <https://doi.org/10.3390/batteries7020022>.
- [21] M. Azzam, C. Endisch, M. Lewerenz, *Batteries* 2024, 10, 3. <https://doi.org/10.3390/batteries10010003>.
- [22] M. C. Schulze, M.-T. F. Rodrigues, J. D. McBrayer, D. P. Abraham, C. A. Applett, I. Bloom, Z. Chen, A. M. Colclasure, A. R. Dunlop, C. Fang, K. L. Harrison, G. Liu, S. D. Minteer, N. R. Neale, D. Robertson, A. P. Tornheim, S. E. Trask, G. M. Veith, A. Verma, Z. Yang, C. Johnson, *J. Electrochim. Soc.* 2022, 169, 50531. <https://doi.org/10.1149/1945-7111/ac6f88>.
- [23] L. Streck, T. Roth, P. Keil, B. Strehle, S. Ludmann, A. Jossen, *J. Electrochim. Soc.* 2023, 170, 40520. <https://doi.org/10.1149/1945-7111/acb669>.
- [24] T. Boetticher, A. Adamson, S. Buechele, E. D. Alter, M. Metzger, *J. Electrochim. Soc.* 2023, 170, 60507. <https://doi.org/10.1149/1945-7111/acd8fd>.
- [25] P. Keil, A. Jossen, *J. Electrochim. Soc.* 2017, 164, A6066–A6074.
- [26] L. Hartmann, L. Reuter, L. Wallisch, A. Beiersdorfer, A. Adam, D. Goldbach, T. Teufel, P. Lamp, H. A. Gasteiger, J. Wandt, *J. Electrochim. Soc.* 2024, 171, 60506. <https://doi.org/10.1149/1945-7111/ad4821>.
- [27] I. Zilberman, J. Sturm, A. Jossen, *J. Power Sources* 2019, 425, 217–226. <https://doi.org/10.1016/j.jpowsour.2019.03.109>.
- [28] J. P. Schmidt, A. Weber, E. Ivers-Tiffée, *J. Power Sources* 2015, 274, 1231–1238. <https://doi.org/10.1016/j.jpowsour.2014.10.163>.
- [29] A. Farmani, D. U. Sauer, *Electrochim. Solid-State Lett.* 2017, 347, 1–13. <https://doi.org/10.1016/j.jpowsour.2017.01.098>.
- [30] B. Rumberg, B. Epding, I. Stradtmann, A. Kwade, *J. Storage Mater.* 2019, 25, 100890. <https://doi.org/10.1016/j.est.2019.100890>.
- [31] S. M. P. Jagfeld, K. P. Birke, A. Fill, P. Keil, *Batteries* 2023, 9, 232. <https://doi.org/10.3390/batteries9040232>.
- [32] W. Waag, S. Käbitz, D. U. Sauer, *Appl. Energy* 2013, 102, 885–897. <https://doi.org/10.1016/j.apenergy.2012.09.030>.
- [33] M. Azzam, M. Ehrensberger, C. Endisch, M. Lewerenz, *J. Storage Mater.* 2024, 102, 114142. <https://doi.org/10.1016/j.est.2024.114142>.
- [34] G. K. Mertin, E. Richter, M. Oldenburger, M. H. Hofmann, D. Wycisk, A. D. Wieck, K. P. Birke, *J. Power Sources* 2021, 498, 229870. <https://doi.org/10.1016/j.jpowsour.2021.229870>.
- [35] L. Spitthoff, M. S. Wahl, J. J. Lamb, P. R. Shearing, P. J. S. Vie, O. S. Burheim, *Batteries* 2023, 9, 249. <https://doi.org/10.3390/batteries9050249>.
- [36] I. Zilberman, A. Rheinfeld, A. Jossen, *J. Power Sources* 2018, 395, 179–184. <https://doi.org/10.1016/j.jpowsour.2018.05.052>.
- [37] G. K. Mertin, D. Wycisk, M. Oldenburger, G. Stoye, A. Fill, K. P. Birke, A. D. Wieck, *J. Storage Mater.* 2022, 51, 104361. <https://doi.org/10.1016/j.est.2022.104361>.
- [38] B. Pattipati, B. Balasingam, G. V. Avvari, K. R. Pattipati, Y. Bar-Shalom, *J. Power Sources* 2014, 269, 317–333. <https://doi.org/10.1016/j.jpowsour.2014.06.152>.

- [39] V. Knap, D.-I. Stroe, *J. Power Sources* **2021**, *498*, 229913. <https://doi.org/10.1016/j.jpowsour.2021.229913>.
- [40] K. Jalkanen, T. Aho, K. Vuorilehto, *Electrochem. Solid-State Lett.* **2013**, *243*, 354–360. <https://doi.org/10.1016/j.jpowsour.2013.05.199>.
- [41] Electrochemical Methods for Determining Kinetic Properties of Solids, W Weppner, and R A Huggins, Vol. 8:269–311 (Volume publication date August 1978) <https://doi.org/10.1146/annurev.ms.08.080178.001413>
- [42] A. Verma, K. Smith, S. Santhanagopalan, D. Abraham, K. P. Yao, P. P. Mukherjee, *J. Electrochem. Soc.* **2017**, *164*, A3380–A3392. <https://doi.org/10.1149/2.1701713jes>.
- [43] M. A. Roscher, O. Bohlen, J. Vetter, *Int. J. Electrochem.* **2011**, *2011*, 1–6. <https://doi.org/10.4061/2011/984320>.
- [44] M. P. Mercer, C. Peng, C. Soares, H. E. Hoster, D. Kramer, *J. Mater. Chem. A* **2021**, *9*, 492–504. <https://doi.org/10.1039/D0TA10403E>.
- [45] P. M. Attia, S. Das, S. J. Harris, M. Z. Bazant, W. C. Chueh, *J. Electrochem. Soc.* **2019**, *166*, E97–E106. <https://doi.org/10.1149/2.0231904jes>.

Manuscript received: September 23, 2024

Revised manuscript received: November 22, 2024

Accepted manuscript online: November 22, 2024

Version of record online: December 11, 2024
